

Article

# Magmatic-Hydrothermal Processes Associated with Rare Earth Element Enrichment in the Kangankunde Carbonatite Complex, Malawi

Frances Chikanda <sup>1,\*</sup>, Tsubasa Otake <sup>2</sup>, Yoko Ohtomo <sup>2</sup>, Akane Ito <sup>1</sup>, Takaomi D. Yokoyama <sup>3,†</sup> and Tsutomu Sato <sup>2</sup>

<sup>1</sup> Graduate School of Engineering, Hokkaido University, N13W8, Kita-ku, Sapporo 060-8628, Japan

<sup>2</sup> Faculty of Engineering, Hokkaido University, N13W8, Kita-ku, Sapporo 060-8628, Japan

<sup>3</sup> Institute for Geo-Resources and Environment, Geological Survey of Japan, National Institute of Advanced Industrial Science and Technology, Central 7, 1-1-1 Higashi, Tsukuba 305-8567, Japan

\* Correspondence: franceschikanda2@gmail.com; Tel.: +81-11-706-6323

† Present affiliation: SA Business Unit, JEOL Ltd., 3-1-2 Musashino, Akishima, Tokyo 196-8558, Japan.

Received: 14 March 2019; Accepted: 14 July 2019; Published: 18 July 2019



**Abstract:** Carbonatites undergo various magmatic-hydrothermal processes during their evolution that are important for the enrichment of rare earth elements (REE). This geochemical, petrographic, and multi-isotope study on the Kangankunde carbonatite, the largest light REE resource in the Chilwa Alkaline Province in Malawi, clarifies the critical stages of REE mineralization in this deposit. The  $\delta^{56}\text{Fe}$  values of most of the carbonatite lies within the magmatic field despite variations in the proportions of monazite, ankerite, and ferroan dolomite. Exsolution of a hydrothermal fluid from the carbonatite melts is evident based on the higher  $\delta^{56}\text{Fe}$  of the fenites, as well as the textural and compositional zoning in monazite. Field and petrographic observations, combined with geochemical data (REE patterns, and Fe, C, and O isotopes), suggest that the key stage of REE mineralization in the Kangankunde carbonatite was the late magmatic stage with an influence of carbothermal fluids i.e. magmatic–hydrothermal stage, when large (~200  $\mu\text{m}$ ), well-developed monazite crystals grew. The C and O isotope compositions of the carbonatite suggest a post-magmatic alteration by hydrothermal fluids, probably after the main REE mineralization stage, as the alteration occurs throughout the carbonatite but particularly in the dark carbonatites.

**Keywords:** carbonatite; REE enrichment; Fe, C, and O isotopes; magmatic-hydrothermal

## 1. Introduction

Rare earth elements (REE) are critical and strategic metals [1] and are becoming increasingly important for industrial use [2], thus warranting further exploration. Among the main types of REE deposits, carbonatites are important exploration targets because of their enrichment in these elements as well as their size and, generally, amenable mineralogy for extraction [3,4]. Although carbonatites exhibit notable enrichments in REE [5], the concentrations vary significantly, depending on the evolutionary processes that they underwent, thereby allowing some carbonatites to be (potential) REE resources (e.g., Barra do Itapirapuã, Brazil [6]; the Mianning-Dechang and Qinling belts, China [7]; Kangankunde, Tundulu, and Songwe, Malawi [8,9]).

Processes that govern the enrichment of REE in carbonatites include fractional crystallization of a carbonatitic melt [10], enrichment by orthomagmatic fluids during late magmatic stages i.e. the magmatic–hydrothermal phase [5], dissolution and re-crystallization of primary to secondary carbonatitic minerals, resulting in the REE being concentrated in the latter [8], and supergene enrichment in weathered zones [11]. Although some studies report that magmatic processes play significant

roles in concentrating the critical elements [4,12], Chakhmouradian and Wall [2] suggest that REE enrichment in carbonatites typically occurs during the final stages of the carbonatite's evolution. During this evolution, overprinting by later magmatic or hydrothermal fluids can also cause further REE enrichment and result in the generation of high-grade deposits, such as Amba Dongar in India [13], Bear Lodge in the USA [14], and Tundulu in Malawi [9]. This contribution focuses on the evolution of the Kangankunde carbonatite, the largest light rare earth (LREE) deposit in the Chilwa Alkaline province, Malawi.

Previous work carried out on the Kangankunde carbonatite includes (i) a detailed geological description of the lithologies present in the complex, highlighting that the REE are mainly concentrated at the centre of the complex [15]; (ii) a description of Mn-rich ankerite along with exotic REE hosting minerals occurring in cavities and vugs, suggesting the precipitation of REE-bearing minerals from orthomagmatic fluids [16]; and (iii) Sr, C, and O isotope compositions of carbonate and phosphate minerals, that suggest that REE mineralization was associated with multi-phase processes occurring at near-magmatic temperatures [5]. Consequently, the processes that were reported on the complex in previous studies may highlight important stages through the evolution of the carbonatite because they play significant roles in concentration of the critical elements [4,12,17]. Despite processes of REE enrichment being characterized for several well-known REE deposits, the processes that generated the prospective Kangankunde carbonatite deposit are still only speculative in nature. Accordingly, this study focuses on the geological-geochemical processes that caused REE enrichment in the Kangankunde Carbonatite Complex.

Monazite is one of the most important REE minerals in carbonatite-related REE deposits [18]. It is abundant in the Kangankunde carbonatite but, interestingly occurs with extremely low Th contents [19]. Although it can occur in both magmatic and hydrothermal systems, it is morphologically different in each setting ranging from euhedral–subhedral crystals to fine-grained polycrystalline aggregates [20], each of which may represent its formation environment. The textural variations of monazite are controlled by thermal, metasomatic, and other geochemical differences [20] during the evolution of the carbonatites [4,21], and therefore have been used as indicators of the evolutionary processes that the carbonatite underwent [4,10,22].

Carbonatites are composed primarily of carbonates, i.e., calcite, (ferroan) dolomite, and ankerite. Since some of the major constituent elements (C, O, and Fe) in these minerals are sensitive to isotopic exchange, they can be utilized as tools to characterize the critical stages of carbonatite formation. Particularly, Fe isotopes have been used to address some significant geological processes through the carbonatites' genesis and evolution [23,24]. Fe isotopes can fractionate as a result of various processes (e.g., the exsolution of Fe<sup>3+</sup>-rich fluids [25], fractional crystallization [26,27], and thermal diffusion [28]), which are prone to occur during magmatic–hydrothermal processes and are also considerably important when understanding the concentration of REE in carbonatites. Despite their significance as geochemical proxies, few studies (e.g., [23,24]) have applied Fe isotopes to characterize the complex interactions between magmatic and hydrothermal processes that occur in carbonatites and may relate to REE enrichment.

By integrating detailed field and petrographic observations with isotope variations (C, O, and Fe), this study aims to (i) characterize the geological–geochemical processes that caused REE enrichment in the Kangankunde Carbonatite Complex, (ii) utilize Fe, C and O isotopes to clarify the stages in the carbonatite evolution and their roles in REE enrichment, and (iii) identify the stage that was most important for REE enrichment.

## 2. Geology of the Kangankunde Carbonatite Complex

### 2.1. Geological Setting

The Kangankunde Carbonatite Complex (Figure 1) is one of the largest REE deposits in the Chilwa Alkaline Complex [14]. The complex has been a target for mineral exploration due to its amenable REE

concentrations hence a detailed description of the complex is given in previous studies [15,29,30]. The Lower Cretaceous Kangankunde complex is aligned N–S parallel to rift valley faults a few kilometers to the west of the East African Rift System [29]. The complex consists of the main complex and a northern and southern knoll. There is a distinct zonation with regards to the lithologies of the main complex. The central core lithology which consists of carbonatite agglomerate is cut by carbonatite dykes and surrounded by a ring of feldspathic breccia and agglomerate [16]. The first intrusion stage comprises apatite–dolomite characteristics and followed by the intrusion of dolomitic to ferroan–dolomitic carbonatite [5]. The apatite-dolomite carbonatite was named beforehand by Garson [15], but the samples that exhibit similar characteristics in our study are named apatite-rich carbonatites because they were not collected from the main apatite body, but most likely from dykes that were too small to map. On the other hand, the terminology from Broom-Fendley et al. [5] is retained in this work, as the samples display similar physical characteristics that were used to name the samples in their study. The Kangankunde Carbonatite Complex is similar to other carbonatites in that it comprises a carbonatite body surrounded by a fenite aureole.

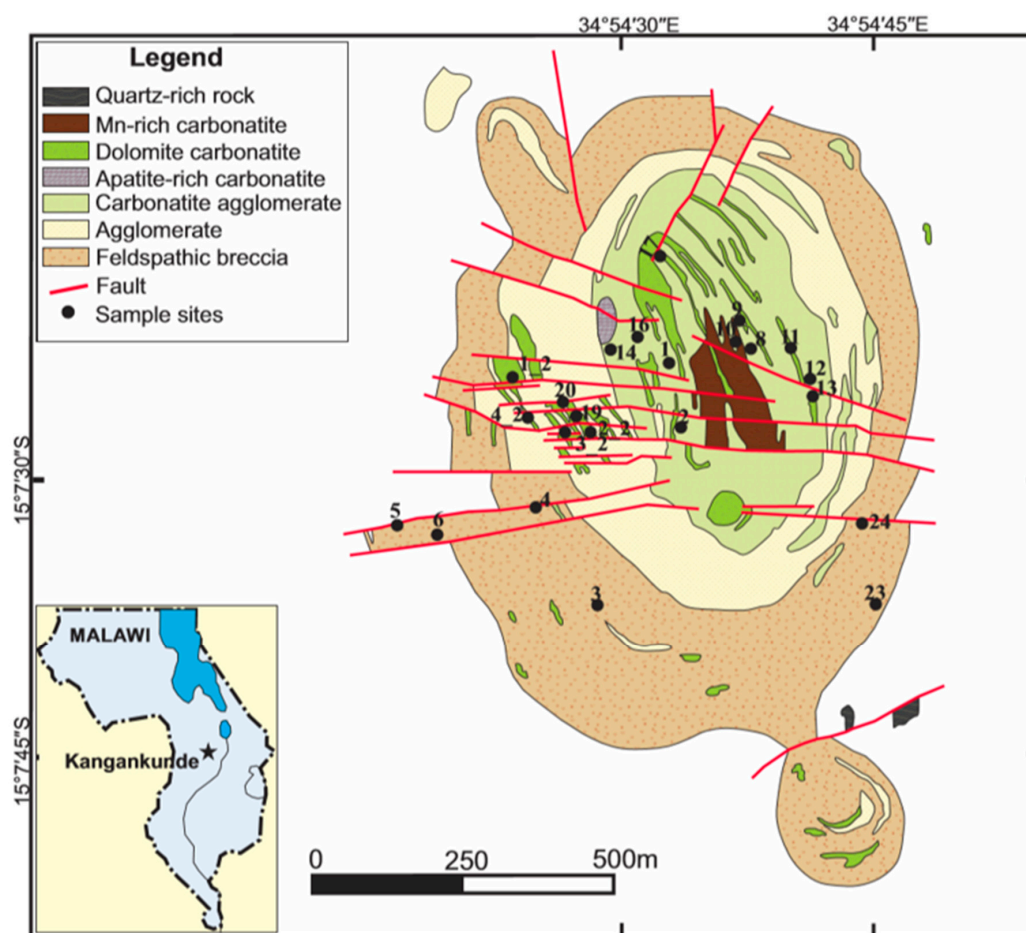


**Figure 1.** Geological map of the Kangankunde carbonatite complex showing sample locations (after Broom-Fendley et al. [5,15]). Inset shows the location of Kangankunde in Malawi, Africa.

## 2.2. Local Geology

The main geological units of the Kangankunde Carbonatite Complex comprise Mn- and REE-rich carbonatites, dolomite carbonatites, apatite-rich carbonatites, carbonatite agglomerate, quartz-rich rocks, and a fenite aureole that surrounds the main carbonatite body. The REE-rich carbonatites are concentrated in the center of the complex, with others occurring irregularly in veins and dykes (commonly as dolomitic and ankeritic carbonatites) that intrude different units of the carbonatite body.

Throughout the complex, outcrops of carbonatite are commonly cut by veins that formed from late (carbothermal) intrusions (Figure 2a,b). Faults occur both regionally and locally in some of the carbonatites of the Chilwa Alkaline Complex. These faults are different from the local faults that developed at Kangankunde, which commonly strike NW and are absent in other carbonatite bodies in the Chilwa Alkaline Province. Well-developed monazite veins of a few cm in width are ubiquitous in the Kangankunde complex and cut carbonatite and fenite breccias (Figure 2c). Carbonatite agglomerates with distinct bulbous textures that resulted from weathering of the carbonate were observed in some lithologies (Figure 2d).

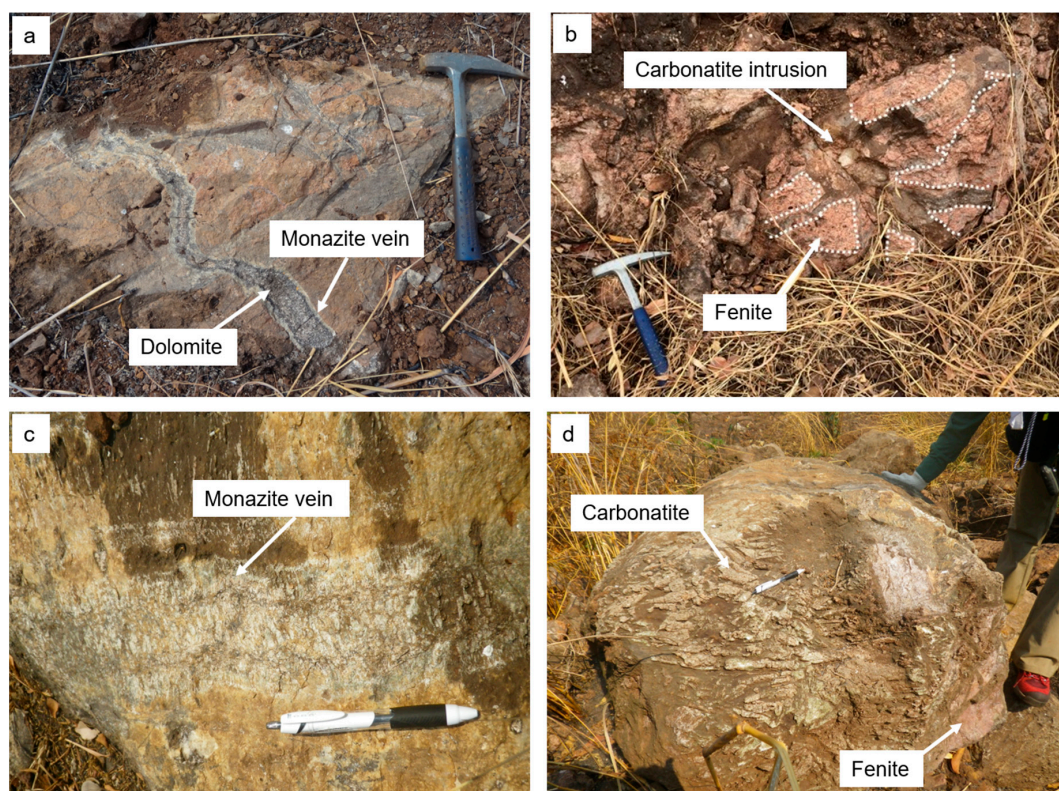


**Figure 2.** Field photographs of carbonatite outcrops at Kangankunde: (a) Zoned dolomite–monazite vein that cuts a carbonatite–fenite breccia, (b) carbonatite intrusion in fenite, (c) monazite vein in a carbonatite breccia displaying unidirectional crystallisation textures, and (d) bulbous breccia of carbonatite and fenite agglomerate.

### 3. Methodology

Samples were acquired from the various lithological units in the Kangankunde Carbonatite Complex to obtain representative samples of mineralized and barren rocks that exhibit the different types of alteration. An extensive sampling program was carried out on the western side of the complex that is prominently fractured and hosts abundant dolomitic intrusions. Although the center of the complex is the main host for highly mineralized carbonatites, the presence of well-developed unidirectional monazite crystals on the west of the complex raised the need of the specific sampling strategy to clarify if the mineralization processes are similar in the various sections of the complex.

Monazite, which is the main host for the REE, imparts a green color to the carbonatites, allowing mineralized rock to be distinguished from barren rock. Samples were collected and classified into light (Figure 3a) and dark (Figure 3b) carbonatites based on their physical appearance [5], apatite-rich carbonatites (Figure 3c), and fenites (Figure 3d). Representative samples were crushed to <75  $\mu\text{m}$  powder for further analysis.

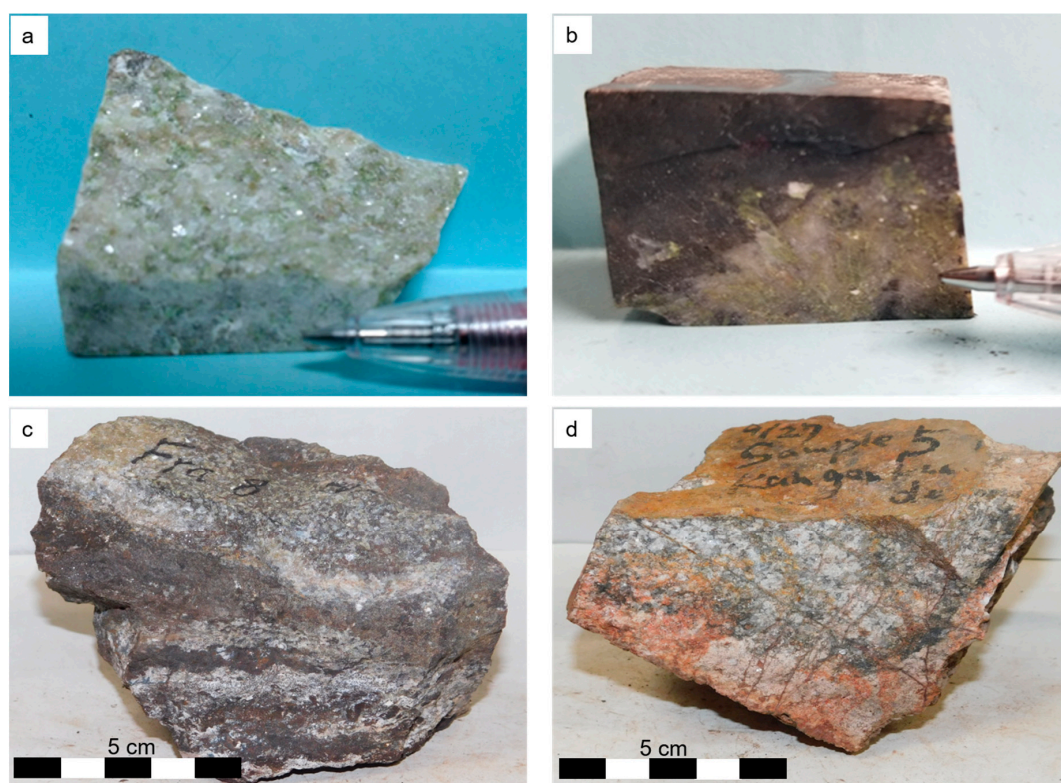


**Figure 3.** Photographs of representative carbonatite samples: (a) Light carbonatite containing polycrystalline monazite, (b) dark ferroan carbonatite containing well-developed monazite crystals, (c) apatite-rich carbonatite showing incipient mineralization, and (d) contact fenite.

Polished thin sections were examined using an Olympus BX60 optical microscope and a JEOL JSM-6510 scanning electron microscope (SEM). The chemical composition of minerals was semi-quantitatively characterized using an energy-dispersive X-ray spectrometer (EDS) operated at an accelerating voltage of 20 kV and beam diameter of  $\sim 5 \mu\text{m}$ . Quantitative mineral compositions were obtained from representative thin sections using a JEOL JXA-8530F electron probe microanalyzer (EPMA, JEOL JXA-8530F) at the Laboratory of Nano-micro Material Analysis, Hokkaido University, Sapporo, Japan. Analyses were obtained using four X-ray detectors and an accelerating voltage of 15 kV, beam current of 20 nA, and beam diameter of  $\sim 5 \mu\text{m}$ . Instrument calibration was achieved by ZAF correction using commercial natural standards of  $\text{LaP}_5\text{O}_{14}$ ,  $\text{CeP}_5\text{O}_{14}$ ,  $\text{NdP}_5\text{O}_{14}$ ,  $\text{SmP}_5\text{O}_{14}$ ,  $\text{EuP}_5\text{O}_{14}$ ,  $\text{GdP}_5\text{O}_{14}$ ,  $\text{DyP}_5\text{O}_{14}$ ,  $\text{ErP}_5\text{O}_{14}$ ,  $\text{YbP}_5\text{O}_{14}$ ,  $\text{YP}_5\text{O}_{14}$ ,  $(\text{Zr}, \text{Y})\text{O}_2$ , and  $\text{CaSiO}_3$  provided by JEOL. Th, Ho, and Pr concentrations were determined by semi-quantitative analysis. All possible overlapping peaks were checked in pre-qualitative analysis.  $L\alpha$  X-ray lines were used for most quantitative analyses except for Sm and Nd concentration, which were determined by  $L\beta$  lines to avoid overlapping with Nd and Ce lines, respectively. Qualitative line analysis was also performed to obtain the concentration variations in the chemically zoned monazite. In the line analysis, peak positions of detected X-ray lines were confirmed using the same commercial standards as quantitative analysis.

Whole-rock major- and trace-element (except REE) compositions were analyzed using a Spectris, MagiX PRO X-ray fluorescence (XRF) spectrometer with a Rh tube. A mixture of 0.4 g of sample powder and 4 g of  $\text{Li}_2\text{B}_4\text{O}_7$  was placed in a platinum crucible, heated at  $1000^\circ\text{C}$  for 8 min in a TK-4100 bead sampler, and then cooled, resulting in fused glass that was used for whole-rock XRF analyses. To avoid erroneous measurements due to incomplete dissolution, the REE concentrations were quantified from the glass bead samples that were initially prepared for XRF, using an Agilent 7700xc inductively coupled plasma–mass spectrometer equipped with a New Wave Research NWR213 laser ablation

sampling system (LA-ICP-MS; Table S1) at the National Institute of Advanced Industrial Science and Technology (AIST), Tsukuba, Japan.

Kangankunde carbonatites have minimal non-carbonate minerals, thereby the C isotopic compositions were taken to represent those of the carbonates, despite the homogenization of the different carbonate generations that may occur. C and O isotope ratios were quantified using a Thermo Scientific Delta V Plus isotope ratio mass spectrometer (IRMS). Powder samples were weighed, with respect to the amount of carbonate carbon contained, in tin containers to minimize sample loss due to electrostatic forces and transferred into 12 mL round-bottomed borosilicate vials [31] that were used to allow uniform flow of the gas to the IRMS. Carbon dioxide was extracted from the whole-rock powders by reaction with 100% phosphoric acid for 1 hour at 70 °C. The oxygen isotope fractionation factor between dolomite and CO<sub>2</sub> gas at 70 °C [32] was used to obtain the δ<sup>18</sup>O value of the carbonate samples. The JLs-1 limestone reference material was used as the laboratory standard (δ<sup>13</sup>C<sub>VDPDB</sub> = 1.92‰ and δ<sup>18</sup>O<sub>SMOW</sub> = 31.09‰). Reproducibility of C and O isotope measurements, based on six analyses of this reference material, was better than 0.1‰ (2σ) for both δ<sup>13</sup>C and δ<sup>18</sup>O values.

Fe isotopes were measured using a Thermo Scientific Neptune Plus multi-collector-ICP-MS (MC-ICP-MS) at the Research Institute for Humanity and Nature, Kyoto, Japan. The procedure for sample digestion using acids was done following the method described as method C by Yokoyama et al. [33], where HCl, HNO<sub>3</sub>, HF, and HClO<sub>4</sub> were used for digesting. Purification of the iron solution was completed by chromatographic separation using columns compacted with anion-exchange resin (AG1-X8 200-400 mesh, Bio-Rad) based on the method of Ito et al. [34]. Solution samples were loaded into the columns with 1 mL of 8 M HCl, and the matrix was removed by 5 mL 8 M HCl and 5 mL of 3 M HCl. Purified Fe eluates were collected with 4 mL of 0.4 M HCl. The purification process was repeated, to improve the purity and multiple passes did not result in Fe isotope fractionations [24]. Finally, samples were redissolved and diluted in 1% HNO<sub>3</sub> to obtain 5 mL of 0.5 ppm Fe solution.

The Fe isotopic compositions were obtained in a middle resolution mode (M/ΔM = 8000–9000) and the instrumental mass bias drift was corrected using the standard-sample-standard bracketing method [23]. Further interferences of <sup>54</sup>Cr<sup>+</sup> on <sup>54</sup>Fe<sup>+</sup> and <sup>58</sup>Ni<sup>+</sup> on <sup>58</sup>Fe<sup>+</sup> were corrected using the isotopic abundances ratios of <sup>54</sup>Cr/<sup>52</sup>Cr = 0.0282 and <sup>58</sup>Ni/<sup>60</sup>Ni = 2.616. The Fe isotopic compositions were assessed using standards and repeated analyses. The isotopic compositions are reported in standard δ-notation (per-mil, ‰) relative to the standard reference material IRMM-014b:

$$\delta^{56}\text{Fe} (\text{‰}) = [({}^{56}\text{Fe}/{}^{54}\text{Fe})_{\text{sample}}/({}^{56}\text{Fe}/{}^{54}\text{Fe})_{\text{IRMM-014b}} - 1] \times 10^3 \quad (1)$$

The reproducibility of the Fe isotopic measurements, based on 9 measurements of the 0.5 ppm Fe standard solution, was typically better than 0.10‰ (2σ).

## 4. Results

### 4.1. Whole-Rock Geochemistry

The major- and trace-element compositions of the carbonatites are summarized in Table A1. Based on the carbonatite classification diagram of Grittins and Harmer [35], which uses the molar proportions of CaO, MgO, and (FeO + MnO), the Kangankunde carbonatite are classified as magnesiocarbonatite and ferrocarnatite (Figure 4). Although a larger group of the carbonatites are compositionally similar to dolomitic carbonatites, the presence of variable amounts of Fe results in a compositional trend towards ankeritic carbonatites. Similar trends were observed for most Kangankunde carbonatite data studied by Broom-Fendley et al. [5]. However, the extension towards Fe-rich end-members is prominent in the samples for this study. The carbonatites from the previous study were classified as mainly REE-rich carbonatites. The apatite-rich carbonatites are compositionally similar to the light and dark carbonatites, but the presence of Ca in the apatite-rich samples causes them to shift slightly towards the CaO region.

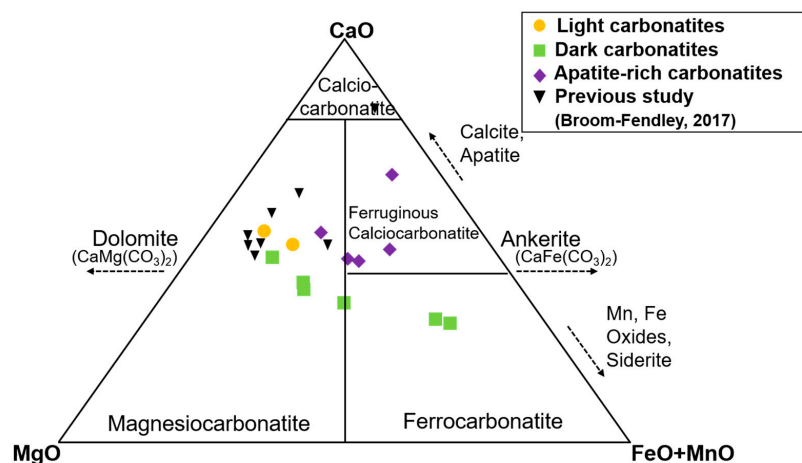


**Figure 4.** Classification of the Kangankunde carbonatites using molar proportions of CaO, MgO, and FeO + MnO (after Grittins and Harmer [35]). Arrows indicate the trends that occur with increasing contents of the specified minerals. Chemical compositions of the Kangankunde carbonatites from a previous study [5] are plotted for comparison.

Most of the Kangankunde carbonatites presented in this study are characterized by high Fe (>16 wt. %), Sr (>20 wt. %), and Ba (>2 wt. %) concentrations (Table A1). In general, P concentration (1–6 wt. %) is positively correlated with total REE (TREE) concentration ( $R^2 > 0.9$ ) (Figure S1) since monazite is the main host mineral for the REE in the Kangankunde carbonatites. The correlation is weaker in the apatite-rich carbonatites given that P (3–12 wt. %) is also controlled by the presence of apatite.

Chondrite-normalized plot of the Kangankunde carbonatite is presented in Figure 5. The Kangankunde carbonatite is generally strongly enriched in LREE (Figure 5), except for the apatite-rich carbonatites, which have shallower slopes on chondrite-normalized REE diagrams due to the higher contents of heavy REE (HREE; Figure 5). In addition, minimal Eu anomalies were observed but none of the carbonatites exhibit Ce anomalies in their REE patterns (Figure 5). While the light carbonatites are less abundant than the dark carbonatites, some of them generally have the highest concentrations of REE. The dark carbonatites are the most abundant throughout the complex and are variably enriched in REE. The apatite-rich carbonatites generally have lower LREE concentrations but have HREE concentrations that are slightly higher than the light and dark carbonatites (Figure 5).

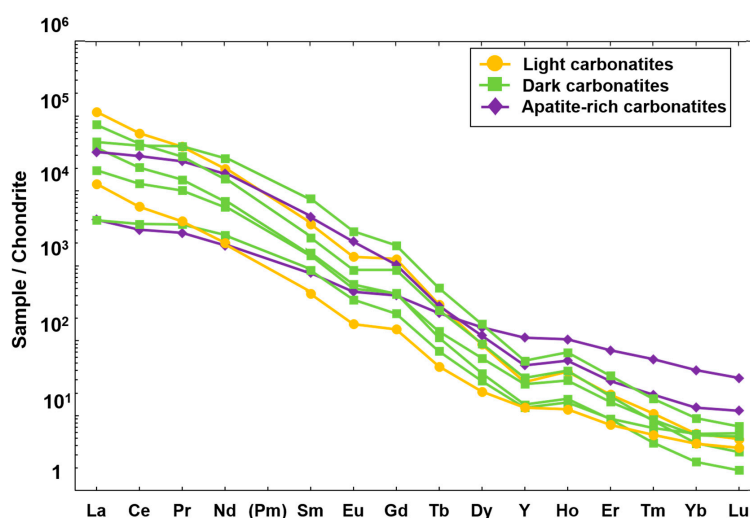


**Figure 5.** Chondrite-normalized REE patterns of the different types of carbonatites in the Kangankunde Carbonatite Complex. Normalization values from McDonough and Sun [36].

#### 4.2. Petrography

The Kangankunde Carbonatite Complex consists primarily of ferroan dolomitic and ankeritic carbonatites, the former are subdivided based on color into light and dark varieties. The carbonatites, which comprise ~70% ferroan dolomite and ankerite, range from pristine to highly altered iron oxides (Figure 6). In the dark carbonatites, the carbonate matrix is mainly ankerite or ferroan dolomite, whereas dolomite is the major carbonate mineral in the light carbonatites. Two types of dark carbonatite are present in the complex. Although both types have been strongly altered into iron oxides, they differ in that one type does not contain monazite or REE mineralization (Figure 6a), whereas the other type does (Figure 6b). Furthermore, the light carbonatites (Figure 6c) comprise mainly euhedral and unaltered dolomite and are comparatively less abundant throughout the complex. In contrast to the carbonate in the light and dark carbonatites, that in apatite-rich carbonatites has been replaced by Fe–Ti oxides in a fluidal pattern (Figure 6d). Iron oxides are present with varying contents of Fe, with the highly altered carbonatites having higher proportions of iron oxides. The iron oxides comprise hematite, goethite, and an unidentified Fe–Mn–Ba-bearing oxide. Calcite is absent in most of the Kangankunde carbonatites, with only minor amounts occurring in the apatite-rich carbonatites. A few other Kangankunde carbonatites that were observed have similar characteristics to the dark carbonatites but are not discussed further as they are categorized as an independent group given their higher proportions of quartz (~26.6%), likely the quartz-rich rocks as previously defined [15].

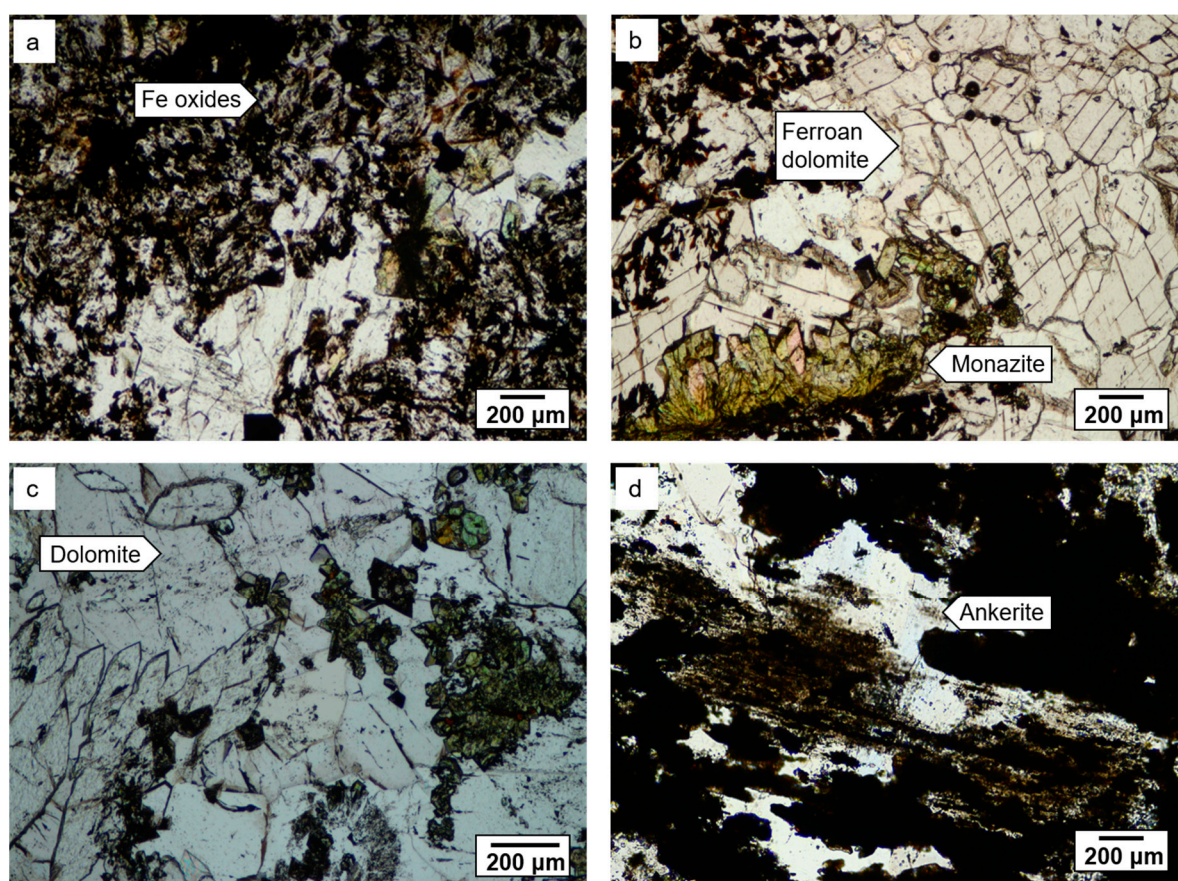


**Figure 6.** Photomicrographs (plane-polarized light) showing the dominant carbonate mineralogy of (a) unmineralized dark carbonatite, (b) mineralized dark carbonatite, (c) light carbonatite, and (d) apatite-rich carbonatite.

The main REE-bearing minerals in the Kangankunde Carbonatite Complex are monazite, bastnaesite, and synchysite. Monazite, which is the most abundant REE-bearing mineral, is green

in hand specimen and exhibits a greenish brown color under plane-polarized light. Two varieties of monazite are present. One variant comprises large (~200  $\mu\text{m}$ ) well-developed crystals that typically occur along the boundaries of dolomite and is commonly observed with abundant iron oxides (Figure 7a). These crystals vary from porous in the core to non-porous in the rim (Figure 7b). The second variant comprises small polycrystalline aggregates of monazite that rarely occur with iron oxides (Figure 7c,d). Bastnaesite and synchysite are less common than monazite and occur as thin needle-like laths (Figure 7e,f) in dolomite.

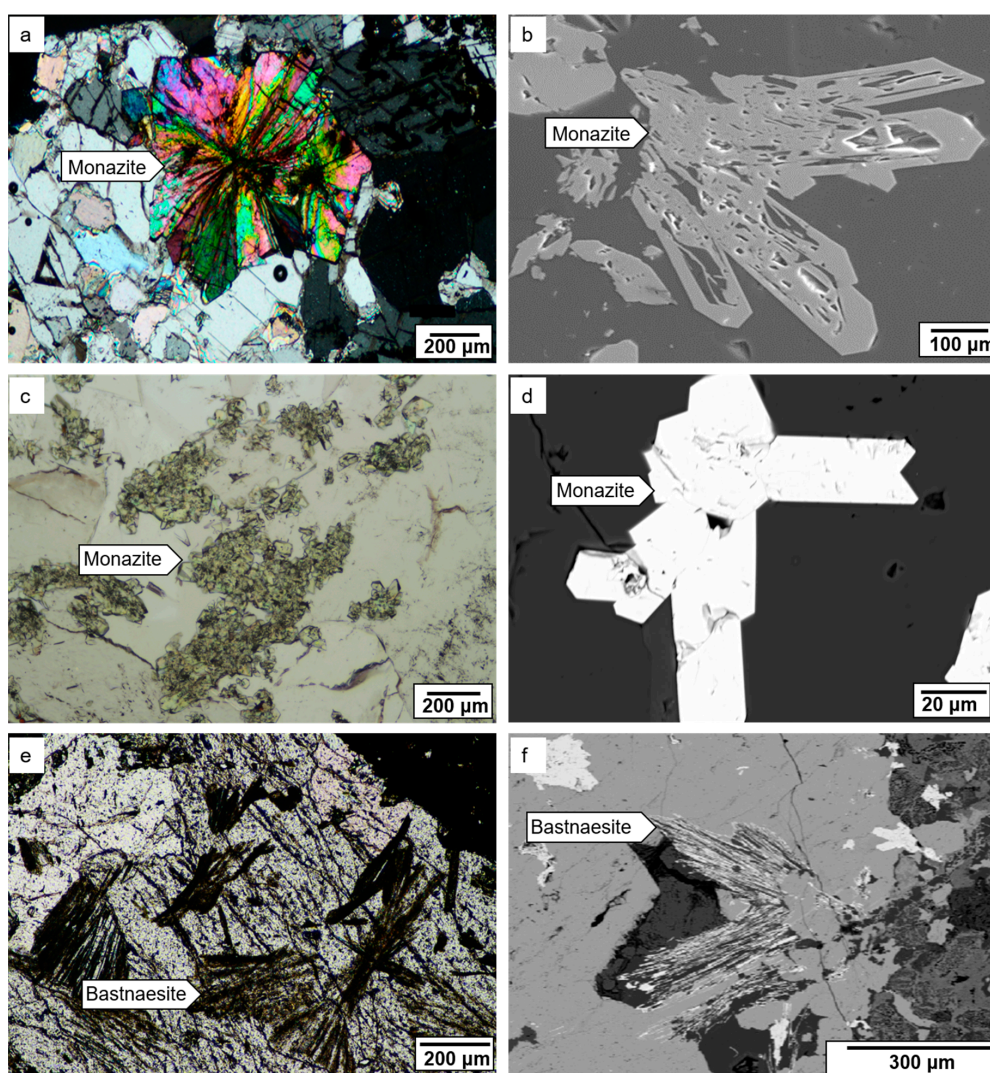


**Figure 7.** (a) Photomicrograph (cross-polarized light) showing a remnant dolomite crystal that was replaced by iron oxides and large monazite crystals. (b) Backscatter electron (BSE) image showing textural zoning in large monazite crystals. Note the porous cores of the crystals. (c) Photomicrograph (plane-polarized light) of small monazite crystal aggregates. (d) BSE image of non-porous monazite crystals from a light carbonatite. (e) Photomicrograph (plane-polarized light) of radiating, needle-like bastnaesite. (f) BSE image of bastnaesite needles.

Furthermore, the large monazite crystals display chemical zoning as shown in the backscattered image in Figure 8 and Table A2. The rims are slightly enriched in HREE (Nd and Sm) compared to the cores. The distribution of LREE is quite homogeneous within the crystal but in minor cases shows a depletion of La and Ce in the rims. Although the texture of the monazite cores can either be porous or non-porous, they are compositionally similar in either case.

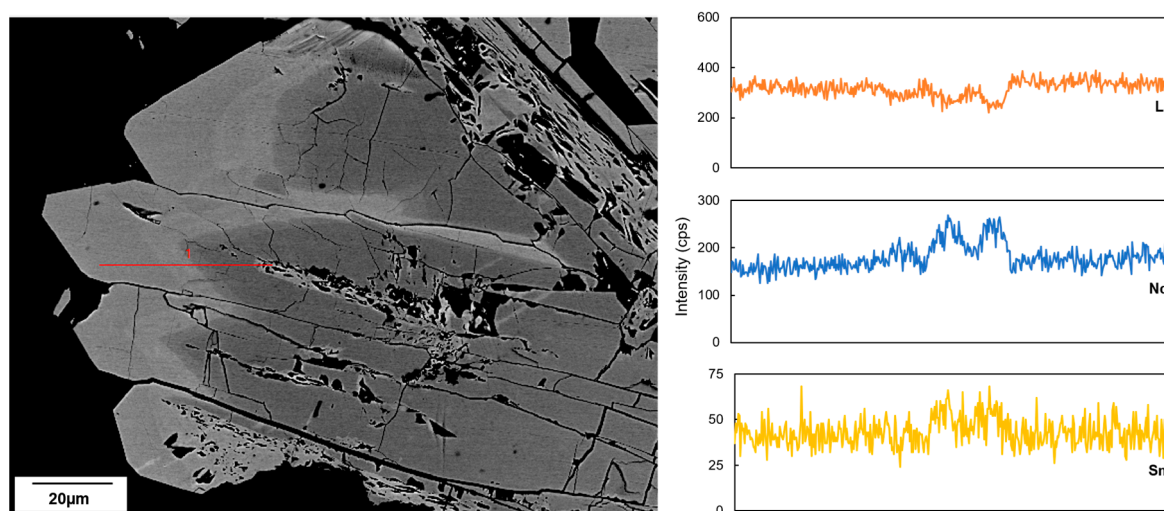


**Figure 8.** Backscatter electron image of texturally and compositionally zoned monazite (left) and compositional variation of REE (La, Nd, and Sm) along the red line on monazite crystal (right).

Strontianite and barite are typically associated with monazite. They generally envelop the monazite or occur along crystal boundaries. Strontianite is typically anhedral and contains trails of fluid inclusions whereas barite typically occurs as euhedral laths (Figure S2). Other minerals in the Kangankunde carbonatites include apatite, quartz, and iron oxides. (Fluor)apatite is most abundant in the apatite-rich carbonatites (Figure S2), but also occurs in minor proportions in the other types of carbonatite. It typically occurs as anhedral ovoid or euhedral hexagonal crystals with minimal zoning. Altered apatite occurs as radiating needles that typically occur in a dolomite matrix.

#### 4.3. Carbon and Oxygen Isotopes

The C and O isotopic compositions of the Kangankunde carbonatites are given in Table A3 and plotted in Figure 9. The  $\delta^{13}\text{C}$  values of the carbonatites ( $-3.98\text{‰}$  to  $0.10\text{‰}$ ) show a smaller variation compared with the  $\delta^{18}\text{O}$  values ( $12.57\text{‰}$  to  $28.94\text{‰}$ ). The large range in  $\delta^{18}\text{O}$  values can be related to the type of carbonatite, with light carbonatites having low  $\delta^{18}\text{O}$ , dark carbonatites having high  $\delta^{18}\text{O}$ , and apatite-rich carbonatites having low to high  $\delta^{18}\text{O}$  values. Furthermore, the light carbonatites form an end member close to the Primary Igneous Carbonatites (PIC) field representing the  $\delta^{13}\text{C}$  and  $\delta^{18}\text{O}$  value ranges for primary, mantle derived carbonatites [21]. Although the data points plotted from a previous study on the Kangankunde carbonatites [5] spread through the plot, they have slightly lower  $\delta^{18}\text{O}$  values in comparison to our sample set. Mineral separates were analyzed for the previous study and the carbonates from the strontianite-rich rock and the beforsite (apatite-rich) plot very close to the PIC field.

#### 4.4. Iron Isotopes

The  $\delta^{56}\text{Fe}$  values for the Kangankunde carbonatites range from  $-0.38\text{‰}$  to  $-0.25\text{‰}$ , with fenite having a value of  $-0.18\text{‰}$  (Table A4). These values are similar to the average  $\delta^{56}\text{Fe}$  value for magmatic carbonatites ( $-0.30\text{‰} \pm 0.05\text{‰}$ ) [23]. No correlation exists between the  $\delta^{56}\text{Fe}$  values and Fe contents of the samples.

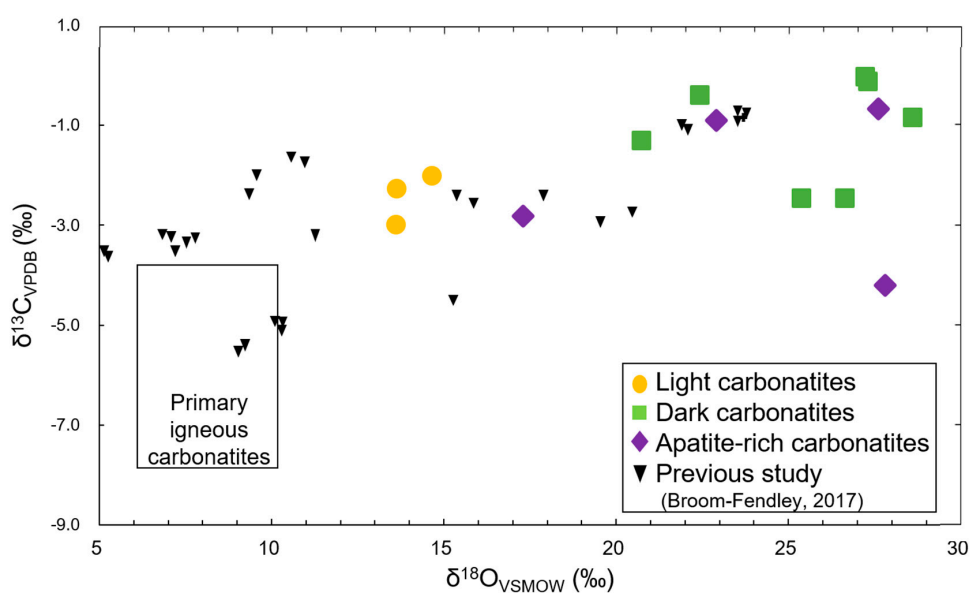


**Figure 9.** Whole-rock  $\delta^{13}\text{C}$  and  $\delta^{18}\text{O}$  compositions of the Kangankunde carbonatites compared with those in a previous study [5]. Compositional fields are shown for primary igneous carbonatites [29].

## 5. Discussion

### 5.1. Evolution of the Carbonatites

The Kangankunde carbonatites exhibit features that are typical of magmatic, magmatic-hydrothermal, and post magmatic processes through their evolution. The minimal alteration in some minerals such as the carbonate in the light carbonatite (Figures 6c and 7d), the small windows of  $\delta^{13}\text{C}$  and  $\delta^{56}\text{Fe}$  isotopic compositions and the geochemistry of some of the carbonatites support a magmatic stage involved in their formation, which corresponds with the interpretation made by Broom-Fendley et al. [5] based on their Sr isotopes. On the other hand, the significantly altered mineralogy in dark and apatite-rich carbonatites, the elevated  $\delta^{18}\text{O}$  isotopic compositions and enrichment of HREE in monazite cores and apatite-rich samples are indicative of the late to post magmatic events through the carbonatites' evolution, also partly reported by Raymond [16] and Broom-Fendley et al. [5].

The carbonatites presented in this study are from various lithologies and focusing on the western section of the complex, which also display high REE concentrations (>2 wt. %). Using the carbonatite classification (Figure 4), these carbonatites spread from magnesiocarbonatite to ferrocarbonatite fields, indicating that they have higher Fe concentrations than most of the carbonatites from the complex that were reported previously [5]. Despite the higher concentrations observed in this study, the light carbonatites have comparatively lower Fe concentrations than the dark and apatite-rich carbonatites. This has been attributed to the breakdown of the ferroan dolomite resulting in darker mineral grains [37] in the dark carbonatite, which supports the occurrence of alteration processes.

However, the Fe isotopic compositions obtained from the carbonatites occur within a very small window ( $-0.38\text{‰}$  to  $-0.26\text{‰}$ , Figure 10), which is within the Fe isotopic range defined for magmatic carbonatites ( $-0.30\text{‰} \pm 0.05\text{‰}$ ) [23,24]. While igneous rocks have demonstrated to have homogenous Fe isotopic compositions [38], high temperature alteration and/or fluid fractionation may result in the fractionation of Fe isotopic values [26,39], hence minimal fractionations would account for significant processes. The evolutionary path (Figure S3) reported for the carbonatite affects the behavior of the REE in the carbonatite, hence the need to clarify the roles of the respective processes on REE enrichment.

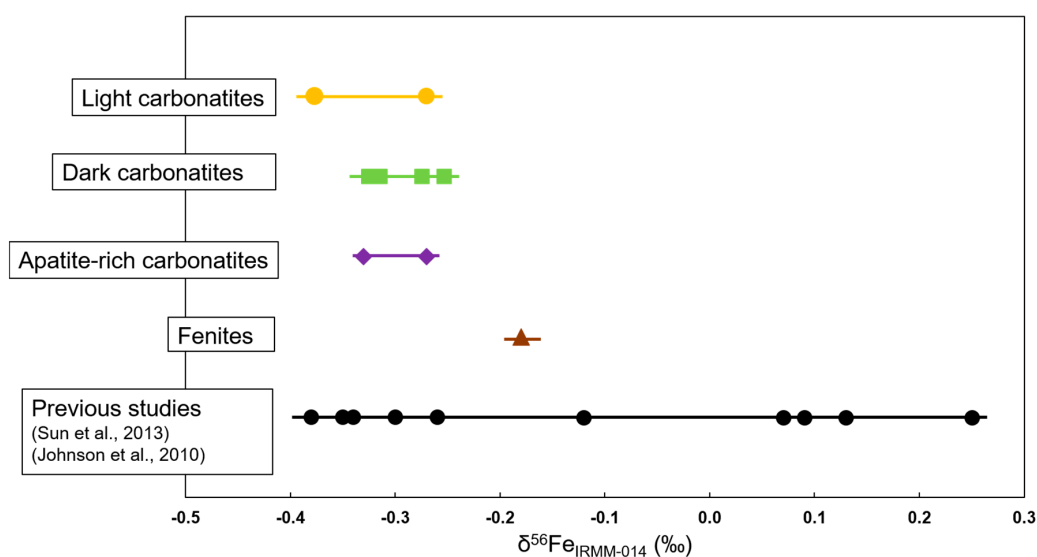


**Figure 10.** Variation in  $\delta^{56}\text{Fe}$  value in the Kangankunde carbonatites. Standard errors ( $2\sigma$ ) for the reference standard and samples were typically better than 0.1‰.

### 5.2. REE Mineralization in the Magmatic Stage

TREE concentrations in the light and dark carbonatites range from 2.53 to 23.71 wt. % and 1.41 to 16.65 wt. %, respectively. Given the magmatic isotopic signatures and minimally altered dolomite of the light carbonatites, the fact that they host significant concentrations of REE suggests that at least some of the REE mineralization occurred during the early magmatic stage despite that REE mineralization in most carbonatites is thought to result from the effects of (carbo-) hydrothermal fluids [3,14,40]. The presence of both apatite and monazite in the Kangankunde carbonatites suggests that the initial magma had high concentrations of P. In addition, the occurrence of REE mineralization in the magmatic stage indicates that the initial magma also had high concentrations of REE. Carbonatite associated REE deposits have been estimated to form from a parent magma that is extremely rich in the REE, along with Sr and Ba [41], which may result in an enrichment of these elements through crustal processes (e.g., liquid immiscibility [40] and subsolidus remobilization [42]). Such a REE-enriched initial magma could have been generated by partial melting of refertilized mantle that had been metasomatized by  $\text{CO}_2$ -rich fluids [43]. Although experimental studies (e.g., [43,44]) have demonstrated that REE mineralization can result from fractional crystallization of carbonatitic melts due to the incompatibility of the REE and other associated elements, it is typical that scarce mineralization occurs during the primary magmatic stage. Accordingly, few REE mineralization events of the Kangankunde carbonatites are magmatic in origin.

### 5.3. Magmatic–Hydrothermal Stages Associated with REE Enrichment

Due to the high susceptibility of carbonatites to metasomatization and alteration [5], magmatic fluids are released through the process, which may result in REE enrichment during alteration. Among others, a close observation on the monazite textural variations observed in the Kangankunde carbonatite provides insight on the mineralization events. The textures exhibited by the monazite (Figure 7) depend on whether they occur in the light or dark carbonatites. Monazite in the light carbonatites is typically small in size and occurs as polycrystalline aggregates, whereas that in the dark carbonatites typically occurs as relatively large and well-developed, hexagonal crystals. This textural variation suggests that the monazites have undergone various stages (e.g., hydrothermal) other than the primary magmatic processes.

The small aggregated textures exhibited by monazite in the light carbonatites (Figure 7) may have resulted from fractional crystallization during the early magmatic stages, as the carbonatites solely

preserves magmatic signatures from petrography and C isotopic compositions, despite occurring outside the PIC field. However, the study area contains late magmatic intrusions (Figure 1) that indicate intricate occurrences during the evolution of the carbonatite which explains the monazite textures in the dark and apatite-rich carbonatites. The large (~200  $\mu\text{m}$ ) monazite crystals in the dark carbonatites, typically occur along the grain boundaries of dolomite, suggesting either that they precipitated from a later fluid or crystallized concurrently with the dolomite. The minor Eu anomalies also suggest formation of monazite in a metamorphic environment [45]. Furthermore, they exhibit homogenous textures and chemical zoning, features typical of ortho- to late-magmatic stages [10].

Monazite can form in metamorphic environments [45–47], as pseudomorphs of other minerals (e.g., burbankite) [5], or as an alteration product during the evolution of minerals such as apatite [48]. The typical crystallization temperature of monazite in a metasomatic environment is ~600 °C [49], which would allow for the formation of well-developed crystals similar to those observed in the Kangankunde dark carbonatites. Broom-Fendley et al. [5] suggested that the monazite crystals in the Kangankunde carbonatites are pseudomorphs that formed from the breakdown of burbankite immediately after its formation, an observation that was confirmed from the clear hexagonal shape of the large the monazite (Figure 8). In addition to the hexagonal shapes, the large monazite crystals display distinct chemical zoning that was not observed in the small aggregates of monazite of the light carbonatites. Monazite crystal variation is known to result from various stages of (re)crystallization, which may cause compositional variations especially after interacting with a hydrothermal fluid [42]. Similar processes may have occurred in the Kangankunde large monazite. The chemical zoning in these crystals was then a result of the reaction with hydrothermal fluids. We therefore suggest that the large monazite crystals formed following an alteration from burbankite, and that compositionally zoned monazite was formed due to the involvement of a hydrothermal fluid at near-magmatic temperatures. This is supported by the occurrence of these monazites as large and well-developed crystals, and by their compositional and textural zoning (Figure 8).

The significance of late-magmatic processes to the generation of REE-enriched minerals has been reported [50]. In the early stages of carbonatite crystallization, fluids typically exsolve from the carbonatite melt due to their high-water contents [25]. These fluids are usually enriched in REE because there is, in general, a low mineral/melt partition coefficient for the REE [13]. In the case of a much later fluid, interaction with a residual magma that had high concentrations of REE may also result in enriched REE concentrations in the fluid phase [13]. Exsolution of a fluid phase rich in  $\text{Fe}^{3+}$ , Cl, F, S, Ca, Mg, or other carbonatite constituents from the carbonatite magma has been stated [51] and, in the Kangankunde carbonatite, is supported by the heavy  $\delta^{56}\text{Fe}$  values in fenites relative to the carbonatites [23,24,52]. Furthermore, significant remobilization signatures are observed in outcrops of the Kangankunde carbonatites (Figure 2a,c) and are particularly prominent in the western region where unidirectional monazite veins are observed, which suggests the presence of a fluid. Studies of carbonatites from Brazil [53] and India [13] have indicated that the late magmatic stages are crucial for the enrichment of REE. Hence, the precipitation of monazite from such an REE-rich fluid could have generated the REE enriched monazites in the Kangankunde carbonatites.

During the early magmatic stages of carbonatite formation, carbothermal fluids enriched in ligands such as  $\text{OH}^-$ ,  $\text{F}^-$ , and  $\text{Cl}^-$  typically exsolve from the carbonatitic magma [17]. Interaction of these fluids with the REE-rich residual magma would generate complexes with the REE, thereby enhancing the formation, transportation, and deposition of large, REE-rich hydrothermal monazite (Figure 7b). Based on the textural and compositional variations observed within the monazite crystals of this study (Figure 8), monazite occurred in multiple stages characterized by differences in pressure, temperature, and fluid composition. These changing conditions would also have affected the uptake of REE by monazite [54]. The occurrence of these monazites along the crystal boundaries of dolomite (Figure 6b), along with the alteration of carbonates (dolomite and/or ankerite) by Fe oxides, further suggests that the large monazite crystals formed as a result of a fluid infusion and possibly remobilization through the earlier formed carbonatites [13].

Within a magmatic–hydrothermal system, it has been suggested that Fe isotopes are fractionated due to (a) exsolution and loss of an aqueous fluid [25,54,55], (b) fractional crystallization, which may also involve changes in redox conditions [56–58], and (c) the effects of thermal diffusion [28,59–61]. These processes commonly occur in magmatic–hydrothermal systems during and after the formation of carbonatites and can be characterized using Fe isotopes [62]. In the Kangankunde carbonatites, Fe is hosted mainly by ankerite and ferroan dolomite, which make up >70% of the carbonatites. Therefore, the fractionation of Fe isotopes reflects the major processes that led to carbonatite formation and, more importantly, to REE mineralization. The concentration of Fe is also notably different between the light and dark carbonatites, with the latter generally having higher concentrations (Figure 4). This compositional difference suggests either that Fe was added to the carbonatite by fluids (alteration of ferroan dolomite by iron oxides in the dark carbonatites) [5], that the light and dark carbonatites crystallized from compositionally distinct magmas (i.e., the dark carbonatite crystallized from a magma that was enriched in Fe) [63], or that the Fe is a product of exsolution in the breakdown of ferroan dolomite. In either case, the concentration of Fe among the different carbonatites varies significantly (Figure 3) and is an important indicator of their evolutionary processes.

The  $\delta^{56}\text{Fe}$  values for the Kangankunde carbonatites (Figure 10) are relatively homogenous ( $-0.38\text{‰}$  to  $-0.26\text{‰}$ ) and indicate only minor fractionation among the carbonatites. The Fe-rich carbonates (dolomite and ankerite) are observed mainly in the dark carbonatites where they are further being replaced by Fe oxides through weathering. Despite the various controls on Fe in the carbonatite, Fe isotopic compositions display minimal fractionations from each other, all within that defined for magmatic carbonatites. This indicates that the major stages responsible for the formation of the carbonatites would have been during the magmatic window.

The difference in isotopic composition of the fenites and carbonatites (Figure 10), however, suggests that partial oxidation and exsolution of an  $\text{Fe}^{3+}$ -bearing fluid with heavier  $\delta^{56}\text{Fe}$  values also played an important role in the evolution of the carbonatite. Exsolution of fluids from the carbonatite melt is consistent with the abundance of large monazite crystals (Figure 7), given that fluid exsolution likely occurred during the magmatic–hydrothermal phase, resulting in further alteration. The presence of the light carbonatites, which strongly preserve signatures of magmatic origin (Figure 9), suggests that during the early phases of carbonatite evolution, several stages might have occurred. These phases may have resulted from different pulses of magma; e.g., an initial pulse that had relatively low Fe contents followed by a subsequent pulse that was relatively enriched in Fe and possibly accompanied by fluid that resulted in alteration. The monazite crystals in the dark carbonatites are well developed, which is common for monazites that crystallize during the magmatic stage [20]. Their large size is a result of the subsequent magma pulses that interacted with magmatic fluids, resulting in only minor  $\delta^{56}\text{Fe}$  fractionation in the carbonatites. Therefore, despite the significant mineralogical and compositional differences among the carbonatites, the REE-bearing carbonatites likely formed during the magmatic-hydrothermal stage. The formation of minor amounts of REE-bearing minerals in the magmatic stage was likely due to the initial carbonatitic magma being relatively enriched in REE.

Crystallization of other minerals during the early stages of carbonatite formation may have generated the minor negative shift of  $\delta^{56}\text{Fe}$  value in some of the samples [23], which likely occurred late in the evolution series. It is evident, however, that significant evolution processes, including REE mineralization, occurred during the magmatic-hydrothermal stages of carbonatite formation. Furthermore, the REE enrichment of the carbonatites on the western side of the complex was enhanced by the magmatic-hydrothermal processes, resulting in the dark carbonatites that are significantly altered in comparison to the light carbonatites.

#### 5.4. Low-Temperature Hydrothermal Overprint

The magmatic  $\delta^{13}\text{C}$  and  $\delta^{18}\text{O}$  signatures of the carbonatites were modified by post-magmatic processes (Figure 9). Compared with  $\delta^{18}\text{O}$ , the  $\delta^{13}\text{C}$  values of the carbonatites are less variable ( $-0.03\text{‰}$  to  $-4.21\text{‰}$ ) and fall within the range of magmatic values but above the range of mantle values

( $\delta^{13}\text{C} = -7.0\text{‰}$  to  $-5.0\text{‰}$ ) [64], suggesting that the magmatic C isotope signature was preserved. The elevated  $\delta^{13}\text{C}$  values compared with those expected of mantle-derived melts was likely caused by near-surface alteration by fluids that were meteoric in origin, possibly after exhumation of the complex [8,65]. In contrast to the  $\delta^{13}\text{C}$  values, the  $\delta^{18}\text{O}$  values (13.61‰ to 28.61‰) are more variable and generally correlate with the physical appearance of the carbonatites, with the light carbonatites having lower values than the dark carbonatites. Fractionation models calculated by Ray and Ramesh [66] and Broom-Fendley et al. [5] suggest that trends towards high O isotopic compositions, similar to those observed in the Kangankunde carbonatites, can result from the alteration of carbonatites by low-temperature fluids. The temperatures predicted for these fluids (<150 to ~250 °C) in a model presented by Broom-Fendley et al. [5] are consistent with the homogenization temperatures obtained from fluid inclusions that were observed in the dominant carbonate minerals in the Kangankunde carbonatites (Figure S4) but seemed to have not been related to the main mineralization event due to their significantly low temperatures and salinities. This is indicative of an overprint by low-temperature fluids that modified the O isotopic composition of the carbonatites, probably after REE mineralization.

## 6. Conclusions

The magmatic and post-magmatic stages that were critical in the enrichment of REE in the Kangankunde carbonatites have been characterized by integrating field and petrographic observations with geochemical and isotopic data. The magmatic origin of the Kangankunde Carbonatite Complex is demonstrated by the presence of pegmatitic minerals and magmatic Fe isotopic signatures. Post-magmatic alteration is demonstrated by complex outcrops, mineral textures and O isotopic signatures. The magmatic processes resulted in the formation of the volumetrically minor light carbonatites, which are variably enriched in REE. Interaction of the residual magma with a magmatic fluid augmented the crystallization of the hydrothermal fluid-related hexagonal, chemically zoned monazite that is abundant in the dark carbonatites, which are notably enriched in REE.

After solidification, the carbonatites were overprinted by low-temperature fluids that were likely meteoric in origin, resulting in the formation of low-temperature alteration signatures and low homogenization temperatures for fluid inclusions. Based on Fe, C, and O isotopes, the formation of the carbonatites and the REE mineralization occurred largely during the early to late magmatic stages, whereas the alteration modified the carbonatites but was not related to REE mineralization. This suggests that late magmatic fluids of the magmatic-hydrothermal stage were critical in the REE enrichment of the Kangankunde carbonatites.

**Supplementary Materials:** The following are available online at <http://www.mdpi.com/2075-163X/9/7/442/s1>, Table S1: Operating conditions for LA-ICP-MS, Figure S1: Correlation of P vs. TREE concentrations in the light and dark carbonatites, Figure S2: Apatite abundance in apatite-rich carbonatites, Figure S3: Paragenetic sequence of mineral occurrence in the Kangankunde carbonatite, and Figure S4: Fluid inclusion in dolomite and the homogenization temperature of most inclusions.

**Author Contributions:** Conceptualization, F.C., T.O., Y.O., A.I. and T.S.; data curation, T.O.; formal analysis, F.C., Y.O., A.I. and T.D.Y.; funding acquisition, T.O.; investigation, F.C. and A.I.; methodology, F.C.; resources, T.S.; supervision, T.O. and Y.O.; validation, T.D.Y. and T.S.; visualization, T.D.Y. and T.S.; writing—original draft, F.C.; writing—review & editing, F.C., T.O., Y.O. and A.I.

**Funding:** This research was supported by a Joint Research Grant for the Environmental Isotope Study to the Research Institute for Humanity and Nature; the “Nanotechnology Platform” Program of the Ministry of Education, Culture, Sports, Science and Technology (MEXT) of Japan; the Japan Society for the Promotion of Science (JSPS) KAKENHI (17H03502) to T.O.; and the Japan International Cooperation Agency (JICA).

**Acknowledgments:** We thank J. Mtegha for his assistance during fieldwork. We also thank A. Matsumoto (XRF), T. Endo (EPMA), K. Suzuki (SEM), K. Sanematsu and D. Araoka (LA-ICP-MS), K.-C. Shin (MC-ICP-MS), and T. Haraguchi (IRMS), for their technical assistance in acquiring chemical and isotopic data. The authors also thank Jindřich Kynický for the editorial handling and three anonymous reviewers for their constructive comments on the manuscript.

**Conflicts of Interest:** The authors declare no conflict of interest.

## Appendix A

Table A1. Major- and trace-element compositions of the Kangankunde carbonatites and fenites.

Major Element Compositions (wt. %)																		
Elements	Standards			Light Carbonatites		Dark Carbonatites					Apatite-Rich Carbonatites					Fenites		
	JB-3	JB-1b	JGb-1	Ka14	Ka20	Ka1	Ka4	Ka12	Ka17	Ka16	Ka19	Ka3	Ka8	Ka10	Ka11	Ka9	Ka6	Ka23
SiO <sub>2</sub>	50.94	51.95	39.86	2.13	10.56	5.93	5.32	2.21	2.91	2.96	34.85	10.22	3.99	18.68	9.66	12.79	70.68	58.02
TiO <sub>2</sub>	1.43	0.77	0.95	b.d	0.14	0.03	0.05	b.d	0.04	0.01	0.40	0.04	b.d	0.04	3.43	0.19	0.27	0.40
Al <sub>2</sub> O <sub>3</sub>	18.20	14.41	17.35	0.05	0.59	0.85	0.52	0.55	0.47	0.05	10.19	1.08	0.14	0.53	1.62	1.39	12.39	13.52
Fe <sub>2</sub> O <sub>3</sub>	7.47	9.03	14.28	6.67	11.61	28.92	25.61	23.25	10.60	16.02	9.99	19.23	13.75	16.14	28.38	21.78	3.90	10.20
MnO	0.18	0.15	0.18	2.31	3.49	6.58	6.97	5.54	3.82	5.08	0.62	4.18	5.15	4.83	1.44	3.18	0.11	0.45
MgO	5.14	8.28	7.34	18.09	16.50	18.40	6.02	24.29	20.56	24.15	8.64	4.05	13.79	5.82	12.57	12.19	0.19	1.57
CaO	10.78	9.65	11.40	34.08	32.68	26.99	13.61	35.88	33.12	38.39	11.86	44.17	35.52	21.21	31.38	28.90	0.26	3.98
Na <sub>2</sub> O	3.77	2.90	1.05	0.28	0.04	0.26	0.54	0.26	0.24	0.35	0.49	0.37	0.40	0.52	0.28	0.33	3.26	4.22
K <sub>2</sub> O	0.97	0.51	3.88	0.00	0.07	0.35	0.20	0.20	0.18	0.01	6.24	0.23	0.01	0.07	0.10	0.73	4.66	6.46
P <sub>2</sub> O <sub>5</sub>	0.29	0.24	0.08	6.75	0.67	1.01	4.76	0.43	4.31	2.14	2.88	3.64	12.82	12.82	9.13	8.48	1.34	0.45
SrO	0.02	0.04	0.03	10.28	53.85	2.99	8.89	1.57	5.99	4.35	2.02	1.29	3.50	1.04	0.66	1.69	0.02	0.13
BaO	0.02	0.05	0.01	1.11	0.26	1.38	7.20	0.73	0.81	0.84	0.25	2.36	0.73	6.74	0.12	0.92	0.90	0.12
TREE	0.01	0.02	0.00	23.71	2.53	4.12	16.50	1.54	16.65	1.93	8.20	7.68	7.38	11.22	1.41	5.02	0.84	0.16
LOI	-	-	-	33.94	34.91	32.63	20.96	38.10	32.43	38.08	39.87	29.28	27.21	14.28	24.41	16.43	4.85	6.87
Total	99.22	97.99	96.53	94.06	78.89	97.08	86.61	96.67	92.90	96.67	94.36	95.65	95.45	97.28	99.39	95.10	98.54	99.74
Trace Element Concentrations (ppm)																		
Sc	31	27	28	27	293	b.d	b.d	5	32	7	b.d	b.d	15	51	3	15	19	36
V	379	220	622	4.01	51.8	199	1260	246	9	200	115	339	116	310	152	61.6	124	114
Cr	55	460	47	525	64	2	533	13	371	404	279	b.d	32	b.d	40	89	23	14
Co	36	39	57	18	21	17	12	12	13	b.d	15	10	15	23	32	0.5	2	b.d
Ni	36	143	18	235	276	140	300	110	161	195	128	146	109	115	84	116	11	15
Cu	191	36	45	444	374	432	394	286	220	203	141	243	247	228	191	153	84	25
Zn	158	77	114	2270	2060	3820	13,000	4920	2960	9280	2580	3880	7550	7110	658	4720	194	1190
Rb	b.d	298	153	709	2400	153	467	93	412	300	155	38	212	18	b.d	122	48	73

Table A1. Cont.

Major Element Compositions (wt. %)																		
Elements	Standards			Light Carbonatites		Dark Carbonatites						Apatite-Rich Carbonatites				Fenites		
	JB-3	JB-1b	JGb-1	Ka14	Ka20	Ka1	Ka4	Ka12	Ka17	Ka16	Ka19	Ka3	Ka8	Ka10	Ka11	Ka9	Ka6	Ka23
Zr	103	120	26	12,800	b.d	3470	13,300	1530	8220	6810	5180	2290	3610	770	1190	3060	215	18
Nb	2.5	6	4	b.d	3560	318	25	b.d	259	188	4700	1110	b.d	3	1650	647	83	170
Pb	6	5	2	b.d	b.d	9	1340	39	b.d	557	49	234	14	60	178	b.d	18	6
Th	4	10	2	73	925	6	b.d	b.d	136	b.d	468	73.1	b.d	b.d	113	105	13	22
La	10	42	4	113,000	12,400	14,000	45,200	4060	76,200	7510	37,700	29,400	27,400	32,900	4120	18,700	3080	399
Ce	24	734	9	58,500	6150	9980	39,900	3590	42,500	4720	20,500	20,300	18,000	29,300	3000	12,500	589	417
Pr	5	8	1	39,000	3930	8640	39,200	3560	28,800	3700	14,000	14,700	13,300	24,900	2730	10,200	2180	361
Nd	18	27	6	19,700	2020	5540	27,200	2570	14,500	2190	7260	8770	8490	16,900	1870	6080	1490	251
Sm	5	5	2	3600	423	1620	7910	869	2370	573	1370	1910	3000	4490	802	1490	456	83
Eu	1	1	0.6	1320	167	677	2880	351	878	249	499	886	1920	2100	453	567	261	50
Gd	5	5	2	1230	143	498	1860	230	879	205	429	493	1090	1030	404	418	146	32
Tb	0.9	0.8	0.3	306	45	167	504	72	255	1	110	174	320	291	235	133	63	18
Dy	5	4	2	89	21	50	167	29	92	36	37	81	106	117	150	58	36	11
Y	13	10	5	28	13	14	54	13	32	16	14	32	26	47	110	26	23	8
Ho	1.	1	0.4	39	12	17	70	15	40	18	17	36	37	54	104	29	21	6
Er	3	2	1	19	8	8	34	9	18	9	9	19	17	29	74	15	16	3
Tm	0.5	0.4	0.3	11	6	5	17	7	9	4	4	12	12	19	57	9	15	4
Yb	3	2	1	6	4	3	9	6	4	3	2	9	7.8	13	40	5	13	3
Lu	0.5	0.4	0.2	5	4	3	7	6	3	2	2	9	7.5	12	32	5	13	4

\* b.d: below detection limit; TREE: Total rare earth elements; LOI: Loss on Ignition.

**Table A2.** Quantitative EPMA data for monazite.

Element	1	3	4	5	7	8	10	11
P <sub>2</sub> O <sub>5</sub>	28.45	27.96	27.88	28.99	29.08	28.59	29.04	27.71
La <sub>2</sub> O <sub>3</sub>	22.09	22.84	23.52	22.85	18.64	22.59	21.12	22.62
Ce <sub>2</sub> O <sub>3</sub>	32.19	30.55	33.68	31.38	32.79	30.43	33.08	33.21
Nd <sub>2</sub> O <sub>3</sub>	8.99	8.86	8.94	8.250	13.31	8.21	10.84	8.03
Sm <sub>2</sub> O <sub>3</sub>	0.69	0.71	0.39	0.45	1.47	0.48	0.91	0.41
Gd <sub>2</sub> O <sub>3</sub>	3.72	3.54	3.89	3.24	3.77	3.64	3.65	3.67
Dy <sub>2</sub> O <sub>3</sub>	0.08	0.03	0.05	0.03	0.02	0.03	0.04	0.02
Ho <sub>2</sub> O <sub>3</sub>	0.00	0.11	0.04	0.18	0.24	0.00	0.08	0.08
Er <sub>2</sub> O <sub>3</sub>	0.00	0.00	0.00	0.15	0.08	0.04	0.00	0.03
ThO <sub>2</sub>	0.16	0.09	0.19	0.00	0.22	0.20	0.00	0.12
Pr <sub>2</sub> O <sub>3</sub>	0.02	0.00	0.02	0.01	0.00	0.03	0.01	0.04
Y <sub>2</sub> O <sub>3</sub>	0.00	0.00	0.01	0.00	0.00	0.00	0.00	0.00
ZrO <sub>2</sub>	0.38	0.32	0.09	0.63	0.04	0.68	0.16	0.22
CaO	0.34	0.33	0.06	0.75	0.59	0.67	0.19	0.06
<b>Total</b>	97.11	95.36	98.76	96.93	100.25	95.59	99.12	96.23

**Table A3.** Stable C and O isotopic compositions of the Kangankunde carbonatites.

Carbonatite Sub-Group	Sample	$\delta^{13}\text{C}_{\text{VPDB}}$ (‰)	$\delta^{18}\text{O}_{\text{VSMOW}}$ (‰)
Light carbonatites	Ka20	-3.00	13.61
	Ka14	-2.28	13.65
	Ka2	-2.01	14.66
Dark carbonatites	Ka1	-0.13	27.32
	Ka16	-0.85	28.61
	Ka12	-0.03	27.25
	Ka4	-2.47	25.40
	Ka13	-2.47	26.65
	Ka17	-1.31	20.75
Apatite-rich carbonatites	Ka9	-0.40	22.43
	Ka3	-4.21	27.81
	Ka8	-0.91	22.91
	Ka10	-0.68	27.61
	Ka11	-2.82	17.31

**Table A4.** Iron isotopic compositions of the Kangankunde carbonatites and fenites.

Carbonatite Subgroup	Sample	Main Fe bearing Mineral	Fe (wt. %)	$\Delta^{56}\text{Fe}$ (‰)	$2\sigma$
Light carbonatites	Ka20	Ferroan Dolomite	11.61	-0.32	0.05
	Ka14	Dolomite	6.67	-0.27	0.12
	Ka2	Dolomite	3.86	-0.38	0.09
Dark carbonatites	Ka12	Dolomite	23.25	-0.31	0.06
	Ka4	Ankerite	25.61	-0.33	0.05
	Ka17	Ankerite	10.60	-0.32	0.06
	Ka4-2	Ankerite	9.86	-0.25	0.05
	Ka3-2	Ankerite	7.43	-0.28	0.06
Apatite-rich carbonatites	Ka8	Ferroan Dolomite	13.75	-0.33	0.07
	Ka10	Ferroan Dolomite	16.14	-0.27	0.14
Fenites	Ka6	Dolomite	3.90	-0.18	0.06

## References

1. Nassar, N.T.; Du, X.; Graedel, T.E. Criticality of the Rare Earth Elements. *J. Ind. Ecol.* **2015**, *19*, 1044–1054. [[CrossRef](#)]
2. Chakhmouradian, A.R.; Wall, F. Rare earth elements: Minerals, mines, magnets (and more). *Elements* **2012**, *8*, 333–340. [[CrossRef](#)]
3. Mariano, A.N. Economic geology of rare earth minerals. *Rev. Mineral.* **1989**, *21*, 309–337.
4. Verplanck, P.L.; Mariano, A.N.; Mariano Anthony, J. Rare earth element ore geology of carbonatites. *Rare Earth Elem. Crit. Elem. Ore Depos.* **2016**, *18*, 5–32.
5. Broom-Fendley, S.; Wall, F.; Spiro, B.; Ullmann, C.V. Deducing the source and composition of rare earth mineralising fluids in carbonatites: Insights from isotopic (C, O,  $^{87}\text{Sr}/^{86}\text{Sr}$ ) data from Kangankunde, Malawi. *Contrib. Mineral. Petrol.* **2017**, *172*, 96. [[CrossRef](#)]
6. Ruberti, E.; Enrich, G.E.R.; Gomes, C.B.; Comin-Chiaramonti, P. Hydrothermal REE fluorocarbonate mineralization at Barra do Itapirapuã, a multiple stockwork carbonate, southern Brazil. *Can. Mineral.* **2008**, *46*, 901–914. [[CrossRef](#)]
7. Liu, Y. Geochemical and mineralogical characteristics of weathered ore in the Dalucao REE deposit, Mianning-Dechang REE Belt, western Sichuan Province, southwestern China. *Ore Geol. Rev.* **2015**, *71*, 437–456. [[CrossRef](#)]
8. Broom-Fendley, S.; Styles, M.T.; Appleton, J.D.; Gunn, G.; Wall, F. Evidence for dissolution-reprecipitation of apatite and preferential LREE mobility in carbonatite-derived late-stage hydrothermal processes. *Am. Mineral.* **2016**, *101*, 596–611. [[CrossRef](#)]
9. Ngwenya, B.T. Hydrothermal rare earth mineralisation in carbonatites of the Tundulu complex, Malawi: Processes at the fluid/rock interface. *Geochim. Cosmochim. Acta* **1994**, *58*, 2061–2072. [[CrossRef](#)]
10. Johannes Giebel, R.; Gauert, C.D.K.; Marks, M.A.W.; Costin, G.; Markl, G. Multi-stage formation of REE minerals in the Palabora Carbonatite Complex, South Africa. *Am. Mineral.* **2017**, *102*, 1218–1233. [[CrossRef](#)]
11. Witt, W.K.; Hammond, D.P.; Hughes, M. Geology of the Ngualla carbonatite complex, Tanzania, and origin of the Weathered Bastnaesite Zone REE ore. *Ore Geol. Rev.* **2019**, *105*, 28–54. [[CrossRef](#)]
12. Hamilton, D.L.; Freestone, I.C.; Dawson, J.B.; Donaldson, C.H. Origin of carbonatites by liquid immiscibility. *Nature* **1979**, *279*, 52–54. [[CrossRef](#)]
13. Doroshkevich, A.G.; Viladkar, S.G.; Ripp, G.S.; Burtseva, M.V. Hydrothermal REE mineralization in the Amba Dongar carbonatite complex, Gujarat, India. *Can. Mineral.* **2009**, *47*, 1105–1116. [[CrossRef](#)]
14. Moore, M.; Chakhmouradian, A.R.; Mariano, A.N.; Sidhu, R. Evolution of rare-earth mineralization in the Bear Lodge carbonatite, Wyoming: Mineralogical and isotopic evidence. *Ore Geol. Rev.* **2015**, *64*, 499–521. [[CrossRef](#)]
15. Garson, M.S. Carbonatites of southern Malawi. *Bull. Geol. Surv. Malawi* **1965**, *15*, 1–128.
16. Duraiswami, R.A.; Shaikh, T.N. Fluid-rock interaction in the Kangankunde Carbonatite Complex, Malawi: SEM based evidence for late stage pervasive hydrothermal mineralisation. *Open Geosci.* **2014**, *6*, 476–491. [[CrossRef](#)]
17. Verplanck, P.L. The Role of Fluids in the Formation of Rare Earth Element Deposits. *Procedia Earth Planet. Sci.* **2017**, *17*, 758–761. [[CrossRef](#)]
18. Zhou, B.; Li, Z.; Chen, C. Global Potential of Rare Earth Resources and Rare Earth Demand from Clean Technologies. *Minerals* **2017**, *7*, 203. [[CrossRef](#)]
19. British Geological Survey. *Mineral Potential of Malawi*; Malawi SDNP: Blantyre, Malawi, 2009; pp. 1–8.
20. Chen, W.; Honghui, H.; Bai, T.; Jiang, S. Geochemistry of Monazite within Carbonatite Related REE Deposits. *Resources* **2017**, *6*, 51. [[CrossRef](#)]
21. Downes, P.J. Stable H–C–O isotope and trace element geochemistry of the Cummins Range Carbonatite Complex, Kimberley region, Western Australia: Implications for hydrothermal REE mineralization, carbonatite evolution and mantle source regions. *Miner. Depos.* **2014**, *49*, 905–932. [[CrossRef](#)]
22. Li, X.C.; Zhou, M.F. Hydrothermal alteration of monazite-(Ce) and chevkinite-(Ce) from the Sin Quyen Fe-Cu-LREE-Au deposit, northwestern Vietnam. *Am. Mineral.* **2017**, *102*, 1525–1541. [[CrossRef](#)]

23. Johnson, C.M.; Bell, K.; Beard, B.L.; Shultis, A.I. Iron isotope compositions of carbonatites record melt generation, crystallization, and late-stage volatile-transport processes. *Mineral. Petrol.* **2010**, *98*, 91–110. [[CrossRef](#)]
24. Sun, J.; Zhu, X.; Chen, Y.; Fang, N. Iron isotopic constraints on the genesis of Bayan Obo ore deposit, Inner Mongolia, China. *Precambrian Res.* **2013**, *235*, 88–106. [[CrossRef](#)]
25. Heimann, A.; Beard, B.L.; Johnson, C.M. The role of volatile exsolution and sub-solidus fluid/rock interactions in producing high  $^{56}\text{Fe}/^{54}\text{Fe}$  ratios in siliceous igneous rocks. *Geochim. Cosmochim. Acta* **2008**, *72*, 4379–4396. [[CrossRef](#)]
26. Schuessler, J.A.; Schoenberg, R.; Sigmarsson, O. Iron and lithium isotope systematics of the Hekla volcano, Iceland—Evidence for Fe isotope fractionation during magma differentiation. *Chem. Geol.* **2009**, *258*, 78–91. [[CrossRef](#)]
27. Teng, F.; Dauphas, N.; Helz, R. Iron Isotope Fractionation Differentiation During Magmatic in Kilauea Iki Lava Lake. *Science* **2008**, *320*, 1620–1622. [[CrossRef](#)] [[PubMed](#)]
28. Zambardi, T.; Lundstrom, C.C.; Li, X.; McCurry, M. Fe and Si isotope variations at Cedar Butte volcano; insight into magmatic differentiation. *Earth Planet. Sci. Lett.* **2014**, *405*, 169–179. [[CrossRef](#)]
29. Garson, M.S.; Campbell, S.W. Carbonatite and agglomeratic vents in the western Shire Valley. Memoir. *Geol. Surv. Malawi* **1965**, *3*, 15–17.
30. Woolley, A.R. Lithosphere metasomatism and the petrogenesis of the Chilwa Province of alkaline igneous rocks and carbonatites, Malawi. *J. Afr. Earth Sci.* **1987**, *6*, 891–898. [[CrossRef](#)]
31. Breitenbach, S.F.M.; Bernasconi, S.M. Carbon and oxygen isotope analysis of small carbonate samples (20 to 100  $\mu\text{g}$ ) with a GasBench II preparation device. *Rapid Commun. Mass Spectrom.* **2011**, *25*, 1910–1914. [[CrossRef](#)]
32. Kusaka, S.; Nakano, T. Carbon and oxygen isotope ratios and their temperature dependence in carbonate and tooth enamel using a GasBench II preparation device. *Rapid Commun. Mass Spectrom.* **2014**, *28*, 563–567. [[CrossRef](#)] [[PubMed](#)]
33. Yokoyama, T.; Makishima, A.; Nakamura, E. Evaluation of the coprecipitation of incompatible trace elements with fluoride during silicate rock dissolution by acid digestion. *Chem. Geol.* **1999**, *157*, 175–187. [[CrossRef](#)]
34. Ito, A.; Otake, T.; Shin, K.C.; Ariffin, K.S.; Yeoh, F.Y.; Sato, T. Geochemical signatures and processes in a stream contaminated by heavy mineral processing near Ipoh city, Malaysia. *Appl. Geochem.* **2017**, *82*, 89–101. [[CrossRef](#)]
35. Gittins, J.; Harmer, R.E. What is ferrocarnatite? A revised classification. *J. Afr. Earth Sci.* **1997**, *25*, 159–168. [[CrossRef](#)]
36. McDonough, W.; Sun, S. The composition of the earth. *Chem. Geol.* **1995**, *120*, 223–253. [[CrossRef](#)]
37. Chai, L.; Navrotsky, A. Synthesis, characterization, and energetics of solid solution along the dolomite-ankerite join, and implications for the stability of ordered  $\text{CaFe}(\text{CO}_3)_2$ . *Am. Mineral.* **1996**, *81*, 1141–1147. [[CrossRef](#)]
38. Beard, B.L.; Johnson, C.M. High precision iron isotope measurements of terrestrial and lunar materials. *Geochim. Cosmochim. Acta* **1999**, *63*, 1653–1660. [[CrossRef](#)]
39. Shahar, A.; Young, E.D.; Manning, C.E. Equilibrium high-temperature Fe isotope fractionation between fayalite and magnetite: An experimental calibration. *Earth Planet. Sci. Lett.* **2008**, *268*, 330–338. [[CrossRef](#)]
40. Yang, K.F.; Fan, H.R.; Santosh, M.; Hu, F.F.; Wang, K.Y. Mesoproterozoic carbonatitic magmatism in the Bayan Obo deposit, Inner Mongolia, North China: Constraints for the mechanism of super accumulation of rare earth elements. *Ore Geol. Rev.* **2011**, *40*, 122–131. [[CrossRef](#)]
41. Hou, Z.; Liu, Y.; Tian, S.; Yang, Z.; Xie, Y. Formation of carbonatite-related giant rare-earth-element deposits by the recycling of marine sediments. *Sci. Rep.* **2015**, *5*, 10231. [[CrossRef](#)]
42. Ling, M.X. Formation of the world's largest REE deposit through protracted fluxing of carbonatite by subduction-derived fluids. *Sci. Rep.* **2013**, *3*, 1776. [[CrossRef](#)]
43. Veksler, I.V.; Petibon, C.; Jenner, G.A.; Dorfman, A.M.; Dingwell, D.B. Trace element partitioning in immiscible silicate-carbonate liquid systems: An initial experimental study using a centrifuge autoclave. *J. Petrol.* **1998**, *39*, 2095–2104. [[CrossRef](#)]

44. Wendlandt, R.F.; Harrison, W.J. Rare earth partitioning between immiscible carbonate and silicate liquids and CO<sub>2</sub> vapor: Results and implications for the formation of light rare earth-enriched rocks. *Contrib. Mineral. Petrol.* **1979**, *69*, 409–419. [[CrossRef](#)]
45. O’Nions, R.K.; Zhu, X.K. Monazite chemical composition: Some implications for monazite geochronology. *Contrib. Mineral. Petrol.* **1999**, *137*, 351–363.
46. Guarino, V.; Wu, F.Y.; Melluso, L.; Gomes, C.B.; Tassinari, C.C.G.; Ruberti, E.; Brilli, M. U–Pb ages, geochemistry, C–O–Nd–Sr–Hf isotopes and petrogenesis of the Catalão II carbonatitic complex (Alto Paranaíba Igneous Province, Brazil): Implications for regional-scale heterogeneities in the Brazilian carbonatite associations. *Int. J. Earth Sci.* **2017**, *106*, 1963–1989. [[CrossRef](#)]
47. Rubatto, D.; Williams, I.S.; Buick, I.S. Zircon and monazite response to prograde metamorphism in the Reynolds Range, central Australia. *Contrib. Mineral. Petrol.* **2001**, *140*, 458–468. [[CrossRef](#)]
48. Zirner, A.L.K.; Marks, M.A.W.; Wenzel, T.; Jacob, D.E.; Markl, G. Rare earth elements in apatite as a monitor of magmatic and metasomatic processes: The Ilímaussaq complex, South Greenland. *Lithos* **2015**, *228*, 12–22. [[CrossRef](#)]
49. Goswami-Banerjee, S.; Robyr, M. Pressure and temperature conditions for crystallization of metamorphic allanite and monazite in metapelites: A case study from the Miyar Valley (high Himalayan Crystalline of Zaskar, NW India). *J. Metamorph. Geol.* **2015**, *33*, 535–556. [[CrossRef](#)]
50. Zaitsev, A.N. Rhombohedral carbonates from carbonatites of the Khibina Massif, Kola Peninsula, Russia. *Can. Mineral.* **1996**, *34*, 453–468.
51. Morogan, V. Mass transfer and REE mobility during fenitization at Alnö, Sweden. *Contrib. Mineral. Petrol.* **1989**, *103*, 25–34. [[CrossRef](#)]
52. Le Bas, M.J.; Xueming, Y.; Taylor, R.N.; Spiro, B.; Milton, J.A.; Peishan, Z. New evidence from a calcite-dolomite carbonatite dyke for the magmatic origin of the massive Bayan Obo ore-bearing dolomite marble, Inner Mongolia, China. *Mineral. Petrol.* **2007**, *90*, 223–248. [[CrossRef](#)]
53. Cordeiro, P.F.; Brod, J.A.; Palmieri, M.; de Oliveira, C.G.; Barbosa, E.S.; Santos, R.V.; Gaspar, J.C.; Assis, L.C. The Catalão I niobium deposit, central Brazil: Resources, geology and pyrochlore chemistry. *Ore Geol. Rev.* **2011**, *41*, 112–121. [[CrossRef](#)]
54. Cressey, G.; Wall, F.; Cressey, B.A. Differential REE uptake by sector growth of monazite. *Mineral. Mag.* **1999**, *63*, 813–828. [[CrossRef](#)]
55. Poitrasson, F.; Freydier, R. Heavy iron isotope composition of granites determined by high resolution MC-ICP-MS. *Chem. Geol.* **2005**, *222*, 132–147. [[CrossRef](#)]
56. Telus, M. Iron, zinc, magnesium and uranium isotopic fractionation during continental crust differentiation: The tale from migmatites, granitoids, and pegmatites. *Geochim. Cosmochim. Acta* **2012**, *97*, 247–265. [[CrossRef](#)]
57. Welch, S.A.; Beard, B.L.; Johnson, C.M.; Braterman, P.S. Kinetic and equilibrium Fe isotope fractionation between aqueous Fe (II) and Fe (III). *Geochim. Cosmochim. Acta.* **2003**, *67*, 4231–4250. [[CrossRef](#)]
58. Sossi, P.A.; Foden, J.D.; Halverson, G.P. Redox-controlled iron isotope fractionation during magmatic differentiation: An example from the Red Hill intrusion, S. Tasmania. *Mineral. Petrol.* **2012**, *164*, 757–772. [[CrossRef](#)]
59. Dauphas, N. Magma redox and structural controls on iron isotope variations in Earth’s mantle and crust. *Earth Planet. Sci. Lett.* **2014**, *398*, 127–140. [[CrossRef](#)]
60. Lundstrom, C. Hypothesis for the origin of convergent margin granitoids and Earth’s continental crust by thermal migration zone refining. *Geochim. Cosmochim. Acta* **2009**, *73*, 5709–5729. [[CrossRef](#)]
61. Huang, F.; Chakraborty, P.; Lundstrom, C.C.; Holmden, C.; Glessner, J.J.G.; Kieffer, S.W.; Leshner, C.E. Isotope fractionation in silicate melts by thermal diffusion. *Nature* **2011**, *464*, 396–400. [[CrossRef](#)]
62. Bilenker, L.D. Elucidating Igneous and Ore-Forming Processes with Iron Isotopes by Using Experimental and Field-Based Methods. Ph.D. Thesis, University of Michigan, Ann Arbor, MI, USA, 2015.
63. Schöpa, A.; Annen, C. The effects of magma flux variations on the formation and lifetime of large silicic magma chambers. *J. Geophys. Res. Solid Earth* **2013**, *118*, 926–942. [[CrossRef](#)]
64. Jones, A.P.; Genge, M.; Carmody, L. Carbonate Melts and Carbonatites. *Rev. Mineral. Geochem.* **2013**, *75*, 289–322. [[CrossRef](#)]

65. Ray, J.S.; Shukla, A.D.; Dewangan, L.K. Carbon and oxygen isotopic compositions of Newania Dolomite Carbonatites, Rajasthan, India: Implications for source of carbonatites. *Mineral. Petrol.* **2010**, *98*, 269–282. [[CrossRef](#)]
66. Ray, J.S.; Ramesh, R. Rayleigh fractionation of stable isotopes from a multicomponent source. *Geochim. Cosmochim. Acta* **2000**, *64*, 299–306. [[CrossRef](#)]



© 2019 by the authors. Licensee MDPI, Basel, Switzerland. This article is an open access article distributed under the terms and conditions of the Creative Commons Attribution (CC BY) license (<http://creativecommons.org/licenses/by/4.0/>).